PCCP

RSC Publishing

PAPER

View Article Online
View Journal | View Issue

Cite this: *Phys. Chem. Chem. Phys.*, 2013, **15**, 18562

Role of central metal ions in hematoporphyrin-functionalized titania in solar energy conversion dynamics

Samim Sardar,[a] Soumik Sarkar,[a] Myo Tay Zar Myint,[b] Salim Al-Harthi,[c] Joydeep Dutta[b] and Samir Kumar Pal*[a]

Received 6th June 2013,
Accepted 12th September 2013

DOI: 10.1039/c3cp52353e

www.rsc.org/pccp

In this study, we have investigated the efficacy of electron transfer processes in hematoporphyrin (HP) and iron hematoporphyrin ((Fe)HP) sensitized titania as potential materials for capturing and storing solar energy. Steady-state and picosecond-resolved fluorescence studies show the efficient photoinduced electron transfer processes in hematoporphyrin–TiO_2 (HP–TiO_2) and Fe(III)-hematoporphyrin–TiO_2 (Fe(III)HP–TiO_2) nanohybrids, which reveal the role of central metal ions in electron transfer processes. The bidentate covalent attachment of HP onto TiO_2 particulates is confirmed by FTIR, Raman scattering and X-ray photoelectron spectroscopy (XPS) studies. The iron oxidation states and the attachment of iron to porphyrin through pyrrole nitrogen atoms were investigated by cyclic voltammetry and FTIR studies, respectively. We also investigated the potential application of HP–TiO_2 and Fe(III)HP–TiO_2 nanohybrids for the photodegradation of a model organic pollutant methylene blue (MB) in aqueous solution under wavelength dependent light irradiation. To further investigate the role of iron oxidation states in electron transfer processes, photocurrent measurements were done by using Fe(III) and Fe(II) ions in porphyrin. This work demonstrates the role of central metal ions in fundamental electron transfer processes in porphyrin sensitized titania and their implications for dye-sensitized device performance.

1. Introduction

The conversion of solar energy to chemical energy during photosynthesis involves the transfer of electrons in porphyrin based chlorophyll chromophores embedded in the thylakoid membranes of the chloroplast.[1] To clarify the complex mechanism of photosynthesis, the photochemistry of porphyrins and their metal complexes has long been an interesting subject of investigation.[2–6] Electron transfer, the most elementary chemical reaction, widely occurs in biological systems.[7–9] The complexity of electron transfer reactions in nature has led researchers to build up simplified model systems to understand the essential steps of the enzyme mechanism in living organisms.[10–12] A significant effort has also been devoted in recent times to the understanding of electron transfer mechanisms as a means of capturing and storing solar energy. The increasing demand for the complete photocatalytic mineralization of organic pollutants in water into harmless products through redox reactions necessitates the exploration of efficient catalysts able to mimic natural enzymatic systems.

Iron porphyrins under sunlight induce reversible redox processes of the metal centre, mimicking some significant biochemical sequences in the catalytic cycle of the cytochrome P-450 oxygenases.[13–15] To reveal the fundamental role of electron transfer processes in biological systems, photoredox reactions of iron porphyrins are very important. The metalloporphyrin excited states that show photochemistry are those involved in charge transfer transitions, either from the axial ligand to the metal centre or from the porphyrin itself to the metal. Due to strong absorption of porphyrins in the region of 400–450 nm (Soret band or B) as well as 500–700 nm (Q bands), they find applications in many fields such as photodynamic therapy for the treatment of cancer[16] and photovoltaic conversion of solar energy.[17–23] The reaction mechanism of porphyrin metallation in solution consists of the following steps: deformation of the porphyrin ring, outer sphere association of the solvated metal ion and the porphyrin, exchange of a solvent molecule with the first pyrrolenine nitrogen atom, and chelatering closure with the expulsion of more solvent molecules followed by deprotonation of nitrogen atoms, which leads to the formation of the metalloporphyrin.[24] The metallation reactions are generally slow processes which can be attributed to

[a] Department of Chemical, Biological and Macromolecular Sciences, S. N. Bose National Centre for Basic Sciences, Block JD, Sector III, Salt Lake, Kolkata 700 098, India. E-mail: skpal@bose.res.in
[b] Chair in Nanotechnology, Water Research Center, Sultan Qaboos University, PO Box 17, 123 Al-Khoudh, Sultanate of Oman
[c] Department of Physics, Sultan Qaboos University, PO Box 17, 123 Al-Khoudh, Sultanate of Oman

the distortion of the porphyrin ring needed to form the first bonds to the metal.[25,26]

Porphyrins anchored on nanocrystalline TiO_2 offer a number of advantages due to its isolation on a solid support: enhancement of its reactivity, inhibition of degradative intermolecular self-reactions and mimicking the proteic environment of the hemeprotein. Colloidal TiO_2 suspensions have been reported extensively for environmental remediation under ultraviolet band light irradiation.[27–29] Bandgap excitations in TiO_2 occur only at wavelengths less than 380 nm, which prevent it from being a potential visible light harvester. Dye sensitization has been successfully applied to extend the spectral response of TiO_2 in the visible region. Organic dyes can serve as both a sensitizer and a substrate to be degraded.[30–32] Many dyes, however, do not sustain the oxidative stress generated on the semiconductor surface.[33] For efficient photocatalysis, the dye has to be stable and regenerative. For example, Zhao *et al.* have reported the degradation of the pollutant 4-chlorophenol by Pt(dcbpy)Cl_2 (dcbpy = 4,4′-dicarboxy-2,2′-bipyridine) incorporated titania under visible light.[34] Porphyrins and metalloporphyrins have been used for the visible light sensitization of TiO_2 and applied for the degradation of 4-nitrophenol, acetaldehyde, rhodamine B, acid chrome blue K, and atrazine.[35–40] Though the photocatalysis using porphyrin and metalloporphyrin functionalized titania is well documented in the literature, knowledge of the fundamental electron transfer dynamics is sparse. The key time scales for the photoinduced ultrafast electron transfer processes in iron porphyrin and its derivatives have great importance due to their biological relevance and also the time scales are the key factor for efficient solar energy conversion. Previously, Zewail and coworkers[41] have reported the femtosecond dynamics of Co(II) tetraphenylporphyrin (CoTPP) and ZnTPP where intramolecular electron transfer from the porphyrin a_{2u} (Л) to Co(d_{z2}) occurs as Co(II) (d^7) facilitates the existence of a low-lying charge transfer (CT) state but in the case of Zn, there is no low-lying CT state as Zn has no unoccupied d orbitals. Granados-Oliveros *et al.*[39] have investigated the photodegradation of atrazine in aqueous solution and under visible light irradiation in the presence of tetra(4-carboxyphenyl)porphyrin (TcPP) with different metal centres (Fe(III), Cu(II), Zn(II) and metal free) adsorbed on the TiO_2 surface. Photocatalytic activity was found only after the addition of hydrogen peroxide and complexes like TcPPFe and TcPPCu containing a central metal ion with unfilled d orbitals show higher photocatalytic activity. Wang *et al.*[42] have reported the efficient degradation of 4-nitrophenol by using 5,10,15,20-tetra-[4-(3-phenoxy)-propoxy]phenyl porphyrin and 5,10,15,20-tetra-[2-(3-phenoxy)-propoxy]-phenyl porphyrin with Cu(II) as the central metal ion under visible light irradiation. They have proposed that the excited electron at the porphyrin LUMO goes to the CB of TiO_2 and then it reduces Cu(II) to Cu(I) and Cu(I) can be reoxidized to Cu(II) by dioxygen species or by hydrogen peroxide produced in solution.

In this work, we have synthesized highly stable nanomaterials, hematoporphyrin–TiO_2 (HP–TiO_2) and Fe(III)-hematoporphyrin–TiO_2 (Fe(III)HP–TiO_2) nanohybrids. Steady-state and picosecond-resolved fluorescence measurements show the ultrafast charge transfer processes in HP–TiO_2 and Fe(III)HP–TiO_2 and we have explored the role of Fe(III) ions in photoinduced electron transfer processes. The attachment of HP molecules to TiO_2 nanoparticles has been investigated by using FTIR, Raman scattering and XPS studies. The iron oxidation states and the attachment of iron to porphyrin through pyrrole nitrogen atoms have been investigated by cyclic voltammetry and FTIR studies, respectively. The photocatalytic activity of these nanomaterials has been studied under wavelength dependent light irradiation. Photocurrent measurements show the role of iron oxidation states in electron transfer processes.

2. Experimental section

Analytical grade chemicals were used for synthesis without further purifications. Fluorine-doped tin oxide (FTO) conducting glass substrates, acquired from *Asahi Glass Company, Japan*, were cleaned by successive sonication with soap water, acetone, ethanol and deionized (DI) water for 15 min each with adequate drying prior to their use.

2.1. Sensitization of HP and Fe(III)HP dyes on the TiO_2 NP surface

A 0.5 mM HP $C_{34}H_{38}N_4O_6$ (Sigma) solution was prepared in anhydrous ethanol under constant stirring at room temperature for 1 h. The sensitization of TiO_2 NPs (Anatase P25) with HP dye was carried out in the dark and at room temperature by adding TiO_2 NPs into a 0.5 mM HP solution with continuous stirring for 12 h. After the sensitization process, the solution was centrifuged for a few minutes and the supernatant clear solution of unattached dyes was removed. Then the sensitized material was washed with ethanol several times to remove any unattached dye. The nanohybrid was then dried in a water bath and stored in the dark until further use. The Fe(III)HP was prepared by adding ferric chloride (Sigma) to the ethanolic solution of HP and stirred for 12 h. The sensitization was done by the same method as described above.

2.2. Characterization methods

Transmission electron microscopy (TEM) grids were prepared by applying a diluted drop of the TiO_2 samples to carbon-coated copper grids. Particle sizes were determined from micrographs recorded at a magnification of 100 000× using an FEI (Technai S-Twin, operating at 200 kV) instrument. For optical experiments, the steady-state absorption and emission were determined using a Shimadzu UV-2450 spectrophotometer and a Jobin Yvon Fluoromax-3 fluorimeter respectively. Picosecond-resolved spectroscopic studies were done using a commercial time correlated single photon counting (TCSPC) setup from Edinburgh Instruments (instrument response function (IRF = 80 ps), excitation at 409 nm). The observed fluorescence transients were fitted by using a nonlinear least square fitting procedure to a function $\left(X(t) = \int_0^t E(t')R(t-t')\,dt'\right)$ comprising convolution of the IRF ($E(t)$) with a sum of exponentials $\left(R(t) = A + \sum_{i=1}^{N} B_i e^{-t/\tau_i}\right)$ with pre-exponential factors (B_i), characteristic lifetimes (τ_i) and a background (A). Relative concentration in a multi-exponential

decay is finally expressed as, $c_n = \frac{B_n}{\sum_{i=1}^{N} B_i} \times 100$. The average lifetime (amplitude-weighted) of a multi-exponential decay is expressed as $\tau_{av} = \sum_{i=1}^{N} c_i \tau_i$. FTIR spectra were recorded on a JASCO FTIR-6300 spectrometer, using a CaF_2 window. Raman scattering measurements were performed by using a LabRAM HR, Jobin Yvon fitted with a Peltier-cooled charge-coupled device (CCD) detector. An air cooled argon ion laser with a wavelength of 488 nm was used as the excitation light source. XPS measurements were carried out using an XPS instrument (Omicron Nanotechnology) with Al K (1486.6 eV). The binding energies of the resultant XPS graphs were calibrated with respect to the C 1s feature at 284.6 eV. The spectra were deconvoluted to the individual components following the Gaussian–Lorentzian function using Casa XPS software. Electrochemical experiments were performed using a CH analyser potentiostat (CHI1110C). For cyclic voltammetry, a three electrode system consisting of a platinum working electrode, a platinum counter electrode and a reference electrode was employed. All the potentials reported in this paper are referenced to the Ag/Ag^+ couple.

2.3. Materials and methods for the VLP process

For the photocatalysis study, HP–TiO_2 and Fe(III)HP–TiO_2 nanohybrids were dispersed in DI water and an aqueous solution of MB in DI water was used as a test contaminant. A 60W UV source was used as the irradiation source in this study. A high pass optical filter (395 nm) was used for visible light irradiation. The mixture of a photocatalyst and a contaminant was irradiated for 1 hour and absorbance data were collected continuously using an ocean optics high resolution spectrometer through a computer interface. The percentage degradation (%DE) of MB was determined using eqn (1):

$$\%\mathrm{DE} = \frac{I_0 - I}{I_0} \times 100 \quad (1)$$

where I_0 is the initial absorption intensity of MB at λ_{max} = 660 nm and I is the absorption intensity after 1 hour of continuous photo-irradiation.

2.4. Langmuir–Hinshelwood (L–H) kinetic model for photocatalytic degradation of MB

The Langmuir–Hinshelwood equation can describe the dependence of [MB] on the degradation rates:

$$R_0 = \frac{\mathrm{d}C}{\mathrm{d}t} = \frac{k_{\mathrm{L-H}} K C_0}{1 + K C_0} \quad (2)$$

where C_0 is the initial concentration of the MB solution, t is the irradiation time, k_{L-H} is the Langmuir–Hinshelwood rate constant, and K is the Langmuir adsorption coefficient of the MB molecules. At lower initial concentrations of MB ($KC_0 \ll 1$), eqn (2) can be simplified to an apparent first order equation:

$$R_0 = k_{\mathrm{L-H}} K C_0 = k_{\mathrm{app}} C_0 \quad (3)$$

where k_{app} is the apparent first-order rate constant. If the initial concentration of MB is sufficiently high ($KC_0 \gg 1$), eqn (2) can be simplified to a zero order rate equation:

$$R_0 = k_{\mathrm{L-H}} \quad (4)$$

2.5. Fabrication of a dye-sensitized solar cell (DSSC) for photocurrent measurements

Photocurrent measurements were done in a dye-sensitized solar cell (DSSC) set up. For the fabrication of DSSCs, platinum NPs deposited on FTO substrates were used as counter electrodes. The platinum (Pt) nanoparticles were deposited on the FTO substrates by thermal decomposition of 5 mM platinum chloride, H_2PtCl_6, H_2O, Fluka, solution in isopropanol at 385 °C for 30 min. HP coated TiO_2 NPs were used as the photoelectrodes and the two electrodes were placed on top of each other with a single layered 50 μm thick Surlyn 1702 (Dupont) as a spacer between the two electrodes. A liquid electrolyte composed of 0.5 M lithium iodide (LiI), 0.05 M iodine (I_2) and 0.5 M 4-tert-butylpyridine (TBP) in acetonitrile was used as the hole conductor and filled in the inter-electrode space by using capillary force, through two small holes (diameter = 1 mm) pre-drilled on the counter electrode. Finally, the two holes were sealed by using another piece of Surlyn to prevent the leakage of electrolyte from the cell. In all our experiments, the active area of the DSSC was fixed at 1 cm^2.[21]

3. Results and discussion

3.1. Characterization of HP–TiO_2 and Fe(III)HP–TiO_2 nanohybrids

A typical high-resolution transmission electron microscopic (HR-TEM) image of TiO_2 NPs showing the polycrystalline nature of the particles is shown in Fig. 1a. The lattice fringe of a TiO_2 NP is illustrated which shows an interplanar distance of ~0.365 nm, corresponding to the spacing between two (101) planes of anatase TiO_2.[43] The particle sizes are estimated by fitting our experimental TEM data over 55 particles which provides the mean diameter of ~6 nm (Fig. 1a, inset). In order to determine the complex formation between the anchoring group of HP and semiconductor NPs, we have conducted studies using UV-vis spectroscopy as shown in Fig. 1b which shows visible light absorption between 400 and 700 nm in HP solution. A strong peak is observed at 397 nm for the Soret band together with Q bands between 500–700 nm. The four weak Q bands have been assigned to the splitting of doubly degenerate states into the vibration components.[44] The HP–TiO_2 nanohybrid exhibits a 3 nm bathochromic shift of the Soret band compared to absorption in HP. The bathochromic shift of the Soret band is related to different physical and chemical changes in the porphyrin molecular structure when it is incorporated into solids or under specific conditions, in solution. Castillero *et al.* have proposed that the red shift with respect to the water solution can be attributed to a change in the environment of the monomeric porphyrin due to the anchoring onto the TiO_2 surface.[45] Sarkar *et al.* have shown that the HP

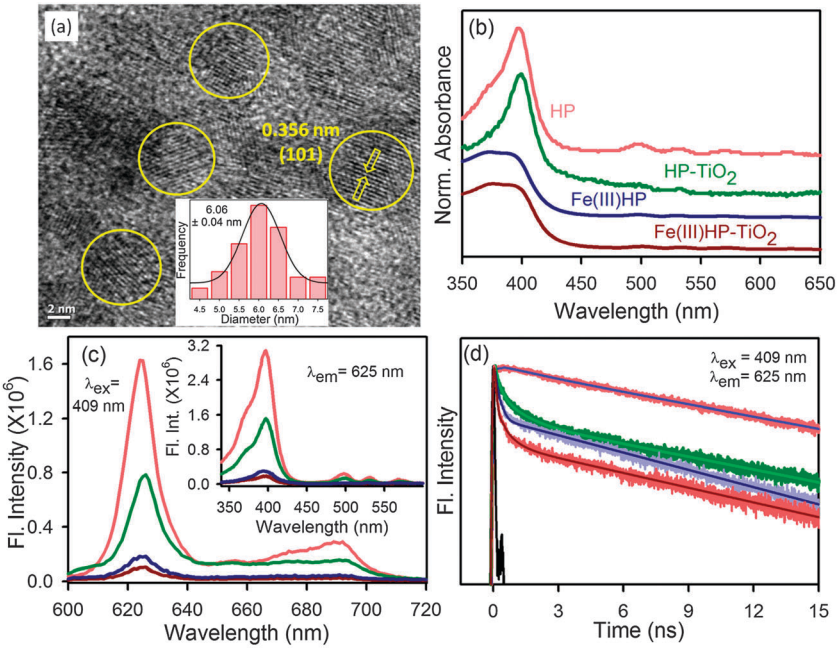

Fig. 1 (a) HRTEM image of TiO_2 NPs. Inset shows the size distribution of the TiO_2 NPs. (b) UV-Vis absorption of HP (red), HP–TiO_2 nanohybrids (dark green), Fe(III)HP (dark blue) and Fe(III)HP–TiO_2 nanohybrids (dark red) in ethanol. (c) Room temperature PL spectra (excitation wavelength was at 409 nm) of bare HP (red), HP–TiO_2 nanohybrids (dark green), Fe(III)HP (dark blue) and Fe(III)HP–TiO_2 nanohybrids (dark red) are shown. Inset shows the excitation spectra monitored at 625 nm. (d) Fluorescence decay profiles of HP (red), HP–TiO_2 nanohybrids (dark green), Fe(III)HP (dark blue) and Fe(III)HP–TiO_2 nanohybrids (dark red) in ethanol.

exhibits a 12 nm bathochromic shift when it attaches to ZnO nanorods.[21] Thus the change in the absorption spectra indicates the formation of the HP–TiO_2 complex.

As shown in Fig. 1c, the HP presents intense fluorescence emission from two pi orbitals, which encompass the basic tetrapyrrole structure upon excitation with a 409 nm laser line. For the HP–TiO_2 nanohybrid, there is a considerable decrease in the intensity of the emission peaks in the range of 600–710 nm as compared to bare HP. The decrease in emission intensities can be attributed to quenching by TiO_2 NPs, suggesting an efficient non-radiative photoinduced process from the HP to the nanoparticles. The inset of Fig. 1c shows the quenching in fluorescence intensity in the excitation spectra of HP upon binding to TiO_2 when monitored at the emission peak (625 nm). The decrease in emission and excitation intensities of HP is also seen in the case of Fe(III)HP and Fe(III)HP–TiO_2 nanohybrids. In Fe(III)HP, intramolecular electron transfer occurs from excited HP to Fe(III) leading to the reduction of Fe(III) to Fe(II).[3]

The fluorescence decays of free HP, Fe(III)HP, HP–TiO_2 and Fe(III)HP–TiO_2 in ethanol were obtained upon excitation of 409 nm laser and monitored at 625 nm (Fig. 1d). The decay curve of free HP is fitted with single exponential decay with a lifetime of 11.39 ns (Table 1). In the case of HP–TiO_2 nanohybrids, the decay curve of HP deviated from single exponential to bi-exponential showing a shorter lifetime 0.40 ns (71%) and longer lifetime 10.68 ns (29%) components. The observed decrease in lifetime could be correlated to the electron transfer process from HP molecules to TiO_2 NPs. The apparent non-radiative rate constant (k_{nr}) is determined by comparing the lifetimes of HP in the absence (τ_0) and in the presence (τ) of TiO_2, using the following equation:

$$k_{nr} = \frac{1}{\langle\tau\rangle} - \frac{1}{\langle\tau_0\rangle} \quad (5)$$

The rate of the electron transfer process from the excited state of HP to the conduction band of semiconductors is estimated to be 2.08×10^8 s^{-1}. The k_{nr} value indicates that the electron transfer process is an ultrafast phenomenon, and it is quite similar to the values reported in the literature.[46] In the case of Fe(III)HP, the decay curve of HP is composed of two components, one shorter 0.14 ns (78%) and one longer 8.43 ns (22%) lifetime

Table 1 Dynamics of picosecond-resolved luminescence transients of HP, Fe(III)HP, HP–TiO_2 and Fe(III)HP–TiO_2 nanohybrids[a]

Sample	τ_1 (ns)	τ_2 (ns)	τ_3 (ns)	τ_{avg} (ns)	$k_{nr} \times 10^8$ (s^{-1})
HP (bare)	11.39 ± 0.01 (100%)			11.39 ± 0.01	
HP–TiO_2	0.40 ± 0.003 (71%)	10.68 ± 0.02 (29%)		3.38 ± 0.01	2.08 ± 0.010
Fe(III)HP	0.14 ± 0.002 (78%)	8.43 ± 0.02 (22%)		1.96 ± 0.003	4.22 ± 0.007
Fe(III)HP–TiO_2	0.09 ± 0.002 (76.4%)	0.40 ± 0.02 (12.5%)	9.74 ± 0.03 (11.1%)	1.19 ± 0.01	7.52 ± 0.060

[a] The emission (monitored at 625 nm) was detected with 409 nm laser excitation. k_{nr} represents nonradiative rate constant. Numbers in the parenthesis indicate relative weightages.

component. The shorter lifetime could be correlated to the electron transfer process from HP to Fe(III) ions. In comparison, the decay curve for Fe(III)HP–TiO_2 has three components, two shorter and one longer component. The shortest component 0.09 ns (76.4%), which is comparable to the shorter component of the decay of Fe(III)HP, shows a preferable electron migration pathway from HP to Fe(III) and the second shorter component, 0.40 ns (12.5%), which is similar to that in the case of HP–TiO_2, could be correlated to the electron transfer process from HP to TiO_2 NPs. It is clear from the lifetime components that the photoinduced excited electrons in HP of Fe(III)HP–TiO_2 preferably transfer to the Fe(III) ions *via* a nonradiative pathway and the electron transfer rate is estimated to be 7.52×10^8 s^{-1}.

The Fourier transform infra-red (FTIR) technique is used to investigate the binding mode of the carboxylate group of HP on the TiO_2 surface. For free HP, stretching frequencies of the carboxylic group are at 1720 cm^{-1} and 1449 cm^{-1} for antisymmetric and symmetric stretching vibrations, respectively, as shown in Fig. 2a. When HP is attached to TiO_2, the stretching frequencies of carboxylic group are located at 1656 and 1453 cm^{-1} for antisymmetric and symmetric stretching vibration, respectively. The difference between carboxylate stretching frequencies, $\Delta = \nu_{as} - \nu_{sym}$ is useful in identifying the bonding mode of the carboxylate ligand.[47] The observed Δ value for the hybrid material is 203 cm^{-1} which is smaller than that for free HP (271 cm^{-1}). This suggests that the binding mode of HP on TiO_2 is predominantly bidentate. The FTIR spectrum of Fe(III)HP–TiO_2 shows that in the presence of iron, HP binds to the TiO_2 NPs through a bidentate covalent bond. FTIR was also used to investigate the attachment of the iron ion to the HP molecule. For free HP, the stretching frequency of the N–H bond is at 3435 cm^{-1}, as shown in Fig. 2b. In the case of the HP–TiO_2 nanohybrid, the N–H stretching frequency of the HP remains unperturbed as HP anchors onto the TiO_2 surface through the carboxylic group. In the presence of iron, the N–H bond is perturbed and becomes broad which indicates that the Fe ion binds to the HP through the pyrrole nitrogen atoms of the porphyrin. After reduction of Fe(III) to Fe(II), FTIR spectra show that the N–H bonds remain broad which indicates that Fe is still inside the porphyrin ring. The iron oxidation states are evaluated by cyclic voltammetry experiments, as shown in Fig. 3. In the presence of Fe(III), a potential for Fe(III)/Fe(II) redox couple is observed at 0.99 V *vs.* Ag/AgCl reference electrode. After treating the Fe(III)HP by sodium borohydride, a reduction potential at −0.35 V was observed which can be attributed to the Fe(II)/Fe(0) redox couple. It is clear that the Fe(III) is reduced to Fe(II) after treating with sodium borohydride.

According to factor group analysis, anatase TiO_2 has six Raman active modes ($A_{1g} + 2B_{1g} + 3E_g$).[48] As shown in Fig. 4a, the Raman spectrum of anatase TiO_2 exhibits six peaks at 150 cm^{-1} (E_g), 198 cm^{-1} (E_g), 396 cm^{-1} (B_{1g}), 515 cm^{-1} (A_{1g}), 520 cm^{-1} (B_{1g}), 640 cm^{-1} (E_g). The Raman spectrum of HP does not show any peak in the wavenumber range of 100–700 cm^{-1}. After binding of HP on the TiO_2 surface, the characteristic bands of TiO_2 are all present but slightly blue shifted and broadened which is indicative of its good retention of the crystal structure and shape.

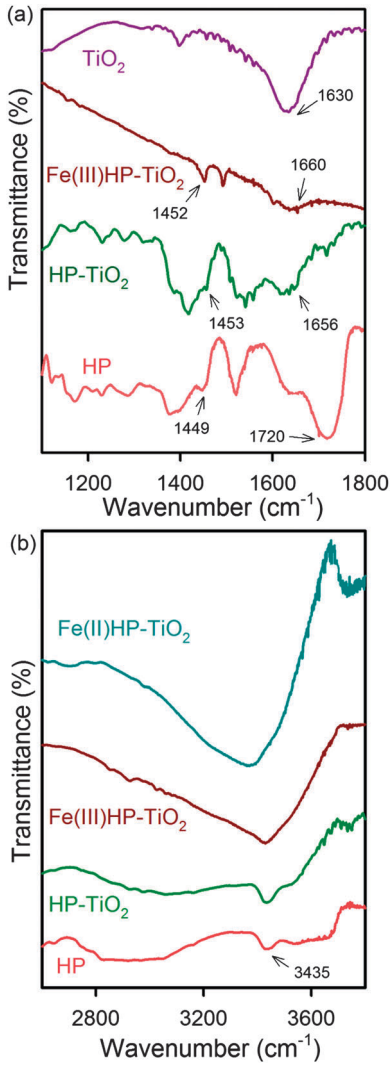

Fig. 2 (a) FTIR spectra of HP (red), TiO_2 NPs (dark pink), HP–TiO_2 (dark green) and Fe(III)HP–TiO_2 (dark red). The spectra of HP–TiO_2 and Fe(III)HP–TiO_2 nanohybrids are taken on TiO_2 background. (b) FTIR spectra of HP (red), HP–TiO_2 (dark green), Fe(III)HP–TiO_2 (dark red) and Fe(II)HP–TiO_2 (dark cyan).

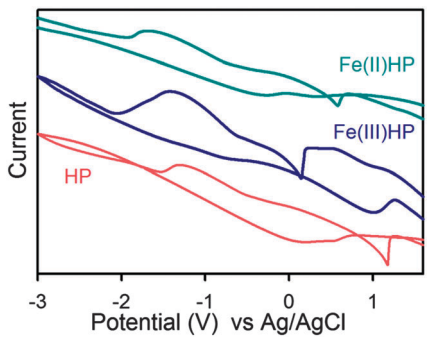

Fig. 3 Cyclic voltammograms of HP (red), Fe(III)HP (dark blue) and Fe(II)HP (dark cyan). The CVs were measured in aqueous solution at 0.1 V s^{-1} scan rate and Ag/AgCl as reference electrode.

In order to see the differences between the spectra more clearly, the wavenumbers and the full width at half maximum (FWHM) of the

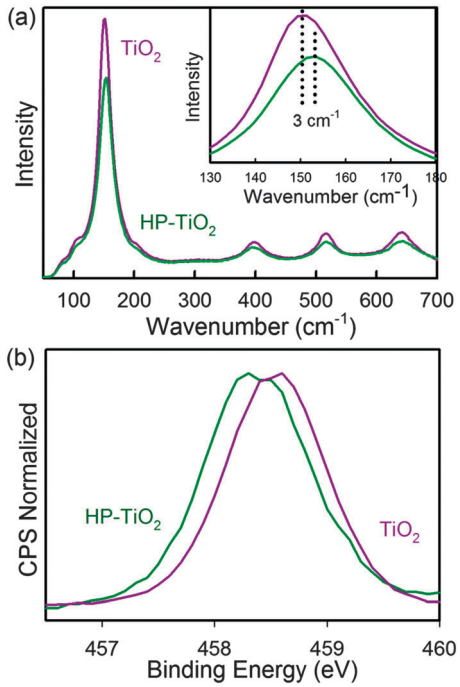

Fig. 4 (a) Raman spectra of TiO_2 NPs (dark pink) and HP–TiO_2 nanohybrids (dark green). Inset shows the peaks at 150 cm^{-1}. (b) XPS of the Ti (2p) regions of TiO_2 (dark pink) and HP–TiO_2 (dark green).

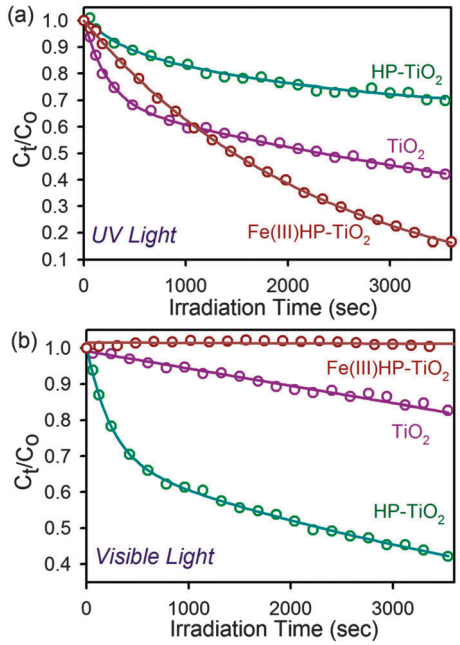

Fig. 5 Photocatalytic degradation of MB in the presence of TiO_2 NPs, HP–TiO_2 and Fe(III)HP–TiO_2 nanohybrids under (a) UV light and (b) visible light.

bands are given in Table 2. Fig. 4a inset shows that the Raman band of TiO_2 at 150 cm^{-1} is shifted to 153 cm^{-1} after binding with HP. The blue shift and broadening of Raman bands of TiO_2 upon binding with HP can be attributed to the attachment of the carboxylic group to Ti(IV) that are located at the TiO_2 surface.

The X-ray photoelectron spectra of the Ti (2p) regions for bare TiO_2 and HP sensitized TiO_2 are shown in Fig. 4b. The Ti ($2p_{3/2}$) binding energy values of TiO_2 and HP–TiO_2 are 458.54 and 458.29 eV respectively. The Ti ($2p_{3/2}$) peak for HP–TiO_2 is shifted to lower binding energy which suggests that the Ti atom as the acceptor coordinates with the oxygen atom in the HP and that the oxygen atom provides electrons.[37] This suggests that HP molecules are adsorbed on the surface of TiO_2 with carboxyl as the coordinating group.

3.2. Photocatalytic activity of HP–TiO_2 and Fe(III)HP–TiO_2 nanohybrids

The irradiation of the HP and Fe(III)HP sensitized TiO_2 suspension with visible light ($\lambda > 395$ nm) led to the degradation of MB in aqueous solution as shown in Fig. 5b. The sensitizer upon excitation with visible light injects electrons to the TiO_2 CB and the subsequent degradation of MB is initiated by transferring CB electrons to MB. The CB electrons can be transferred to MB adsorbed on the TiO_2 surface which leads to the reduction of MB to its leuco form. Thus proximity between MB and the TiO_2 surface plays an important part in photodegradation. The CB electrons can also induce reactive oxygen species (ROS) formation. This sort of remote bleaching is well evidenced in the literature. For example Li *et al.* used porphyrin sensitized TiO_2 photocatalysts to degrade acid chrome blue *K* and the degradation mechanism was shown to follow the ROS pathway.[37]

The photocatalytic degradation of MB in the presence of HP–TiO_2 nanohybrids, Fe(III)HP–TiO_2 nanohybrids and TiO_2 under ultraviolet and visible light was investigated. Under ultraviolet irradiation, 58% MB is degraded in the presence of TiO_2 whereas in the presence of HP–TiO_2 nanohybrids only 30% MB is degraded after 1 h irradiation of light, as shown in Fig. 5a. Under UV irradiation, the TiO_2 valence band (VB) electrons are excited to the conduction band which can reduce dioxygen to superoxide, eventually leading to the production of hydroxyl radicals ($OH^{\bullet}$). The HP molecules that are attached to TiO_2 surface cannot simply withstand this severe oxidative stress and it is also degraded. HP acts as an electron scavenger and decreases the MB degradation rate. In the presence of Fe(III)HP–TiO_2 nanohybrids, 83% MB is degraded after 1 h of UV irradiation. The higher degradation rate can be attributed to the presence of Fe(III)HP which can improve the separation of photoinduced e^-–h^+ pairs.[38] The Fe(III) ion plays an important role in the electron transfer process. Under UV light, TiO_2 VB electrons are excited to the CB and Fe(III) could be reduced to the Fe(II) by capturing the CB electrons of TiO_2. The reoxidation of Fe(II) to

Table 2 Raman bands and FWHM of TiO_2 and HP–TiO_2

Sample	Raman band (cm^{-1})	FWHM (cm^{-1})
TiO_2	150	21
	396	33
	515	27
	640	38
HP–TiO_2	153	24
	397	36
	517	29
	642	42

Fe(III) occurs by reducing oxygen to superoxide, eventually leading to the production of hydroxyl radicals ($OH^{\bullet}$). The following set of reactions explains the enhanced photocatalytic behavior in the presence of Fe(III).

$$\text{Fe(III)HP–TiO}_2 + h\nu \rightarrow \text{Fe(III)HP–TiO}_2\ (e_{cb}^{-}, h^{+}) \quad (6)$$

$$\text{Fe(III)HP–TiO}_2 + e_{cb}^{-} \rightarrow \text{Fe(II)HP–TiO}_2 \quad (7)$$

$$\text{Fe(II)HP–TiO}_2 + O_2 \rightarrow \text{Fe(III)HP–TiO}_2 + \dot{O}_2^{-} \quad (8)$$

Under visible light irradiation, the HP–TiO_2 nanohybrid shows highly efficient photocatalytic activity. After 1 h of irradiation it degrades 60% of MB, whereas under same conditions bare TiO_2 degraded only 16% of MB. Visible light excites the HP molecules attached to TiO_2 and then the electrons from the LUMO of the HP are injected into the CB of TiO_2. Since the rate of electron injection is much faster than the back electron transfer (from TiO_2 to HP), which leads to a null reaction, the electrons in the CB can be transferred onto a substrate on the TiO_2 surface. For example, Desilvestro *et al.* reported that the rate of electron injection ($k_{inj} = 3.2 \times 10^7\ s^{-1}$) in the $Ru^{II}L_3$–TiO_2 system is 80 times faster than the back electron transfer ($k_b = 4 \times 10^5\ s^{-1}$).[49] The regeneration of the sensitizer in the presence of suitable electron donors is a prerequisite for the development of practical photosensitization systems. Water in the media acts as an electron donor to regenerate the surface bound sensitizer molecules, which eliminate the need for any undesirable sacrificial electron donors. In the presence of Fe(III)HP–TiO_2, no MB degradation occurred after 1 h under visible light irradiation. In this case, the photoexcited electrons of the HP are transferred to the Fe(III) ions instead of TiO_2, which is evident from the TCSPC studies as shown in Fig. 1c. The back electron transfer from Fe(II) to HP takes only a few femtoseconds (~50 fs).[50] Thus Fe(III)HP–TiO_2 shows no photocatalytic activity under visible light irradiation.

In Fig. 6, MB degradation rate on the HP sensitized TiO_2 and bare TiO_2 surface under visible-light and UV-light, respectively, are investigated as a function of MB concentration. The R_0 *versus* C_0 curves are fitted using eqn (2). The values of K and $k_{L\text{–}H}$ are given in Table 3. The Langmuir adsorption coefficient of MB molecules for bare TiO_2 (0.08 μmol dm^{-3}) is much higher than that for the HP–TiO_2 nanohybrid (0.05 μmol dm^{-3}) which is obvious because in HP–TiO_2 nanohybrids, the TiO_2 surface sites are less available for MB attachment as HP is already attached to it. The Langmuir–Hinshelwood rate constant for HP–TiO_2 (1.90 μmol dm^{-3} min^{-1}) is higher compared to bare TiO_2 suspension (0.80 μmol dm^{-3} min^{-1}). This phenomenon can be attributed to the higher quantum yield of porphyrin sensitized TiO_2 than that of bare TiO_2 suspension.[51,52]

3.3. Photocurrent measurements and the role of iron oxidation states

The photocurrent measurement of HP–TiO_2 and (Fe)HP–TiO_2 nanohybrids were carried out in order to better understand the electron transfer processes in terms of short circuit current in a solar cell. Photocurrent measurements were done by using the DSSC set up as shown in Fig. 7a. The light source (10 mW cm^{-2}) was turned on and off every 20 s and the obtained current values were continuously recorded. Fig. 7b shows the photocurrent response of HP, Fe(III)HP and Fe(II)HP sensitized TiO_2, where in the presence of Fe(III), photocurrent was found to decrease when compared to the electrodes sensitized with HP. This agrees well with our observations from the TCSPC and photocatalysis experiments. Photoexcited electrons from HP are transferred to Fe(III) instead of TiO_2 in the case of Fe(III)HP sensitized TiO_2 which leads to a decrease in the photocurrent response. When Fe(III) is reduced to Fe(II), the photocurrent increases which indicates that the electrons from the excited HP could be favorably transferred to the TiO_2 CB.

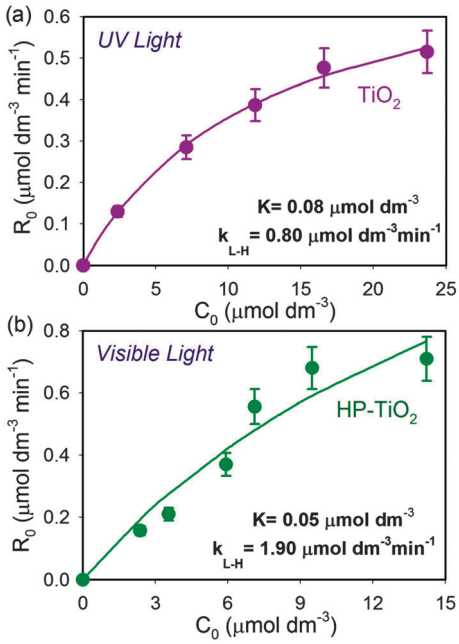

Fig. 6 Degradation rate (R_0) *versus* initial MB concentration (C_0) plots (with 10% error bar): (a) in the presence of TiO_2 NPs under UV light and (b) in the presence of HP–TiO_2 nanohybrids under visible light.

Table 3 Kinetic fitting parameters of Langmuir–Hinshelwood model[a]

Sample	[MB] (μmol dm^{-3})	R_0 (μmol dm^{-3} min^{-1})	K (μmol dm^{-3})	$k_{L\text{–}H}$ (μmol dm^{-3} min^{-1})
Bare TiO_2	2.37	0.129	0.08	0.80
	7.11	0.285		
	11.85	0.387		
	16.59	0.476		
	23.70	0.515		
HP–TiO_2	2.37	0.157	0.05	1.90
	3.55	0.210		
	5.93	0.371		
	7.11	0.556		
	9.48	0.680		
	14.22	0.710		

[a] R_0 is the degradation rate, $k_{L\text{–}H}$ is the Langmuir–Hinshelwood rate constant, and K is the Langmuir adsorption coefficient.

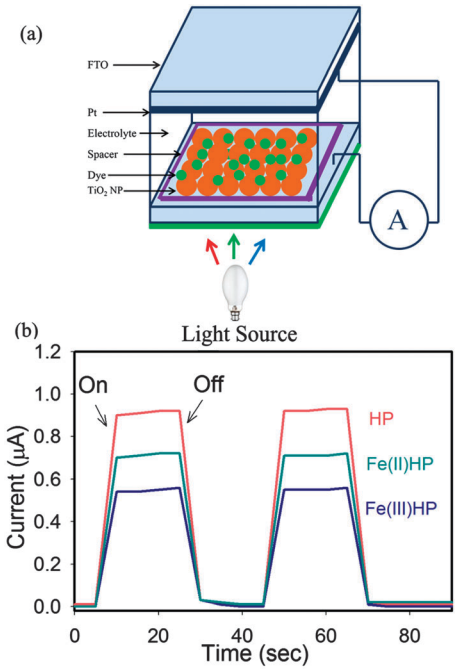

Fig. 7 (a) Schematic representation of photocurrent measurement set up using dye-sensitized solar cell geometry. (b) Photocurrent responses of HP (red), Fe(III)HP (dark blue) and Fe(II)HP (dark cyan) sensitized TiO_2 without any bias voltage under 10 mW cm^{-2} incident power irradiation from a light source.

4. Conclusion

In summary, we have investigated the efficacy of electron transfer processes in hematoporphyrin (HP) and iron hematoporphyrin ((Fe)HP) sensitized titania as a means of harvesting solar energy. The efficient quenching of HP fluorescence in steady state and picosecond-resolved fluorescence measurements in the presence of Fe(III) ions and TiO_2 NPs suggest that photoinduced electron transfer takes place from the LUMO of the HP to the Fe(III) and CB of TiO_2 in Fe(III)HP–TiO_2 and HP–TiO_2 nanohybrids, respectively. These studies reveal the role of central metal ions in the electron transfer processes. Under UV light irradiation, the Fe(III)HP–TiO_2 nanohybrid shows higher photocatalytic activity due to the cooperative functions of Fe(III)HP and TiO_2 in generating active species. HP–TiO_2 nanohybrids show higher photocatalytic activity under visible light due to the absence of Fe(III) ions which obstruct the electron transfer from HP to TiO_2. The bidentate covalent binding between TiO_2 and carboxylic groups of HP has been confirmed by the FTIR, Raman scattering and XPS studies. The iron oxidation states and the attachment of iron to porphyrin through pyrrole nitrogen atoms have been investigated by cyclic voltammetry and FTIR studies, respectively. Photocurrent measurements show the role of iron oxidation states in electron transfer processes.

Acknowledgements

S.S. thanks UGC (India) for fellowship. We thank DST (India) for financial grants DST/TM/SERI/2k11/103 and SB/S1/PC-011/2013. Partial support from the Research Council of Oman is gratefully acknowledged by the authors from SQU. The authors would like to thank Dr Achintya Singha of Bose Institute (India) for providing Raman Scattering measurement facility used in this study.

References

1 K. Sauer, *Acc. Chem. Res.*, 1980, **13**, 249–256.
2 K. S. Suslick and R. A. Watson, *New J. Chem.*, 1992, **16**, 633–642.
3 A. Maldotti, R. Amadelli, C. Bartocci, V. Carassiti, E. Polo and G. Varani, *Coord. Chem. Rev.*, 1993, **125**, 143–154.
4 W. D. Edwards, B. Weiner and M. C. Zerner, *J. Phys. Chem.*, 1988, **92**, 6188–6197.
5 Y. Ozaki, K. Iriyama, H. Ogoshi and T. Kitagawa, *J. Am. Chem. Soc.*, 1987, **109**, 5583–5586.
6 C. Bartocci, F. Scandola, A. Ferri and V. Carassiti, *J. Am. Chem. Soc.*, 1980, **102**, 7067–7072.
7 J. L. Dempsey, J. R. Winkler and H. B. Gray, *Chem. Rev.*, 2010, **110**, 7024–7039.
8 R. H. Holm, P. Kennepohl and E. I. Solomon, *Chem. Rev.*, 1996, **96**, 2239–2314.
9 P. de Rege, S. Williams and M. Therien, *Science*, 1995, **269**, 1409–1413.
10 J.-M. Lehn, *Angew. Chem., Int. Ed. Engl.*, 1988, **27**, 89–112.
11 L. Que and W. B. Tolman, *Nature*, 2008, **455**, 333–340.
12 D. Astruc, *Nat. Chem.*, 2012, **4**, 255–267.
13 A. Maldotti, L. Andreotti, A. Molinari and V. Carassiti, *JBIC, J. Biol. Inorg. Chem.*, 1999, **4**, 154–161.
14 D. Ricard, M. L'Her, P. Richard and B. Boitrel, *Chem.–Eur. J.*, 2001, **7**, 3291–3297.
15 N. Hessenauer-Ilicheva, A. Franke, D. Meyer, W.-D. Woggon and R. van Eldik, *Chem.–Eur. J.*, 2009, **15**, 2941–2959.
16 E. A. Lissi, M. V. Encinas, E. Lemp and M. A. Rubio, *Chem. Rev.*, 1993, **93**, 699–723.
17 A. Yella, H.-W. Lee, H. N. Tsao, C. Yi, A. K. Chandiran, M. K. Nazeeruddin, E. W.-G. Diau, C.-Y. Yeh, S. M. Zakeeruddin and M. Grätzel, *Science*, 2011, **334**, 629–634.
18 L.-L. Li and E. W.-G. Diau, *Chem. Soc. Rev.*, 2013, **42**, 291–304.
19 M. J. Griffith, K. Sunahara, P. Wagner, K. Wagner, G. G. Wallace, D. L. Officer, A. Furube, R. Katoh, S. Mori and A. J. Mozer, *Chem. Commun.*, 2012, **48**, 4145–4162.
20 T. Bessho, S. M. Zakeeruddin, C.-Y. Yeh, E. W.-G. Diau and M. Grätzel, *Angew. Chem.*, 2010, **122**, 6796–6799.
21 S. Sarkar, A. Makhal, T. Bora, K. Lakhsman, A. Singha, J. Dutta and S. K. Pal, *ACS Appl. Mater. Interfaces*, 2012, **4**, 7027–7035.
22 N. Masi Reddy, T.-Y. Pan, Y. Christu Rajan, B.-C. Guo, C.-M. Lan, E. Wei-Guang Diau and C.-Y. Yeh, *Phys. Chem. Chem. Phys.*, 2013, **15**, 8409–8415.
23 T. Hasobe, *Phys. Chem. Chem. Phys.*, 2010, **12**, 44–57.
24 Y. Shen and U. Ryde, *Chem.–Eur. J.*, 2005, **11**, 1549–1564.
25 M. Inamo, N. Kamiya, Y. Inada, M. Nomura and S. Funahashi, *Inorg. Chem.*, 2001, **40**, 5636–5644.
26 S. Funahashi, Y. Inada and M. Inamo, *Anal. Sci.*, 2001, **17**, 917–927.
27 O. Legrini, E. Oliveros and A. M. Braun, *Chem. Rev.*, 1993, **93**, 671–698.

28 M. A. Fox and M. T. Dulay, *Chem. Rev.*, 1993, **93**, 341–357.
29 M. R. Hoffmann, S. T. Martin, W. Choi and D. W. Bahnemann, *Chem. Rev.*, 1995, **95**, 69–96.
30 A. Mills, A. Belghazi, R. H. Davies, D. Worsley and S. Morris, *J. Photochem. Photobiol., A*, 1994, **79**, 131–139.
31 C. Anderson and A. J. Bard, *J. Phys. Chem.*, 1995, **99**, 9882–9885.
32 K. Vinodgopal, D. E. Wynkoop and P. V. Kamat, *Environ. Sci. Technol.*, 1996, **30**, 1660–1666.
33 H. Ross, J. Bendig and S. Hecht, *Sol. Energy Mater. Sol. Cells*, 1994, **33**, 475–481.
34 W. Zhao, Y. Sun and F. N. Castellano, *J. Am. Chem. Soc.*, 2008, **130**, 12566–12567.
35 S. Rodrigues, K. T. Ranjit, S. Uma, I. N. Martyanov and K. J. Klabunde, *Adv. Mater.*, 2005, **17**, 2467–2471.
36 A. A. Ismail and D. W. Bahnemann, *ChemSusChem*, 2010, **3**, 1057–1062.
37 D. Li, W. Dong, S. Sun, Z. Shi and S. Feng, *J. Phys. Chem. C*, 2008, **112**, 14878–14882.
38 H. Huang, X. Gu, J. Zhou, K. Ji, H. Liu and Y. Feng, *Catal. Commun.*, 2009, **11**, 58–61.
39 G. Granados-Oliveros, E. A. Páez-Mozo, F. M. Ortega, C. Ferronato and J.-M. Chovelon, *Appl. Catal., B*, 2009, **89**, 448–454.
40 M.-y. Duan, J. Li, G. Mele, C. Wang, X.-f. Lü, G. Vasapollo and F.-x. Zhang, *J. Phys. Chem. C*, 2010, **114**, 7857–7862.
41 H. Z. Yu, J. S. Baskin, B. Steiger, C. Z. Wan, F. C. Anson and A. H. Zewail, *Chem. Phys. Lett.*, 1998, **293**, 1–8.
42 C. Wang, J. Li, G. Mele, G.-M. Yang, F.-X. Zhang, L. Palmisano and G. Vasapollo, *Appl. Catal., B*, 2007, **76**, 218–226.
43 V. Shklover, M. K. Nazeeruddin, S. M. Zakeeruddin, C. Barbé, A. Kay, T. Haibach, W. Steurer, R. Hermann, H. U. Nissen and M. Grätzel, *Chem. Mater.*, 1997, **9**, 430–439.
44 R. C. Srivastava, V. D. Anand and W. R. Carper, *Appl. Spectrosc.*, 1973, **27**, 444–449.
45 P. Castillero, J. R. Sánchez-Valencia, M. Cano, J. M. Pedrosa, J. Roales, A. Barranco and A. n. R. González-Elipe, *ACS Appl. Mater. Interfaces*, 2010, **2**, 712–721.
46 A. Kathiravan, P. S. Kumar, R. Renganathan and S. Anandan, *Colloids Surf., A*, 2009, **333**, 175–181.
47 G. B. Deacon and R. J. Phillips, *Coord. Chem. Rev.*, 1980, **33**, 227–250.
48 H. C. Choi, Y. M. Jung and S. B. Kim, *Vib. Spectrosc.*, 2005, **37**, 33–38.
49 J. Desilvestro, M. Graetzel, L. Kavan, J. Moser and J. Augustynski, *J. Am. Chem. Soc.*, 1985, **107**, 2988–2990.
50 S. Franzen, L. Kiger, C. Poyart and J.-L. Martin, *Biophys. J.*, 2001, **80**, 2372–2385.
51 L. Sun and J. R. Bolton, *J. Phys. Chem.*, 1996, **100**, 4127–4134.
52 A. Brune, G. Jeong, P. A. Liddell, T. Sotomura, T. A. Moore, A. L. Moore and D. Gust, *Langmuir*, 2004, **20**, 8366–8371.

